Nuclear Inst. and Methods in Physics Research, A 907 (2018) 46–59

Contents lists available at ScienceDirect

Nuclear Inst. and Methods in Physics Research, A

journal homepage: www.elsevier.com/locate/nima

# Detectors for extreme luminosity: Belle II

I. Adachi [a,b], T.E. Browder [c], P. Križan [d,e,*], S. Tanaka [a,b], Y. Ushiroda [a,b,f], (on behalf of the Belle II Collaboration)

[a] High Energy Accelerator Research Organization (KEK), Tsukuba, Japan
[b] SOKENDAI (The Graduate University for Advanced Studies), Hayama 240-0193, Japan
[c] University of Hawaii, Honolulu, HI, United States
[d] Faculty of Mathematics and Physics, University of Ljubljana, Slovenia
[e] Jožef Stefan Institute, Ljubljana, Slovenia
[f] Department of Physics, Graduate School of Science, University of Tokyo, Japan

ARTICLE INFO

*Keywords:*
Belle II
Super B Factory
SuperKEKB
Magnetic spectrometer
Flavor physics

ABSTRACT

We describe the Belle II detector at the SuperKEKB electron–positron accelerator. SuperKEKB operates at the energy of the $\Upsilon(4S)$ resonance where pairs of $B$ mesons are produced in a coherent quantum mechanical state with no additional particles. Belle II, the first Super B factory detector, aims to achieve performance comparable to the original Belle and BaBar B factory experiments, which first measured the large CP violating effects in the $B$ meson system, with much higher luminosity collisions and larger beam-induced backgrounds.

**Contents**



## 1. Introduction

The $B$ factory experiments, Belle and BaBar, discovered large CP violating effects in the $B$ meson sector and provided experimental confirmation of the Kobayashi–Maskawa hypothesis: a single complex phase can explain all the CP violating effects in the weak interaction. This was recognized by the 2008 Nobel Prize in Physics. The emphasis

* Corresponding author at: Faculty of Mathematics and Physics, University of Ljubljana, Slovenia.
*E-mail address:* peter.krizan@ijs.si (P. Križan).

https://doi.org/10.1016/j.nima.2018.03.068
Received 23 March 2018; Accepted 25 March 2018
Available online 12 May 2018

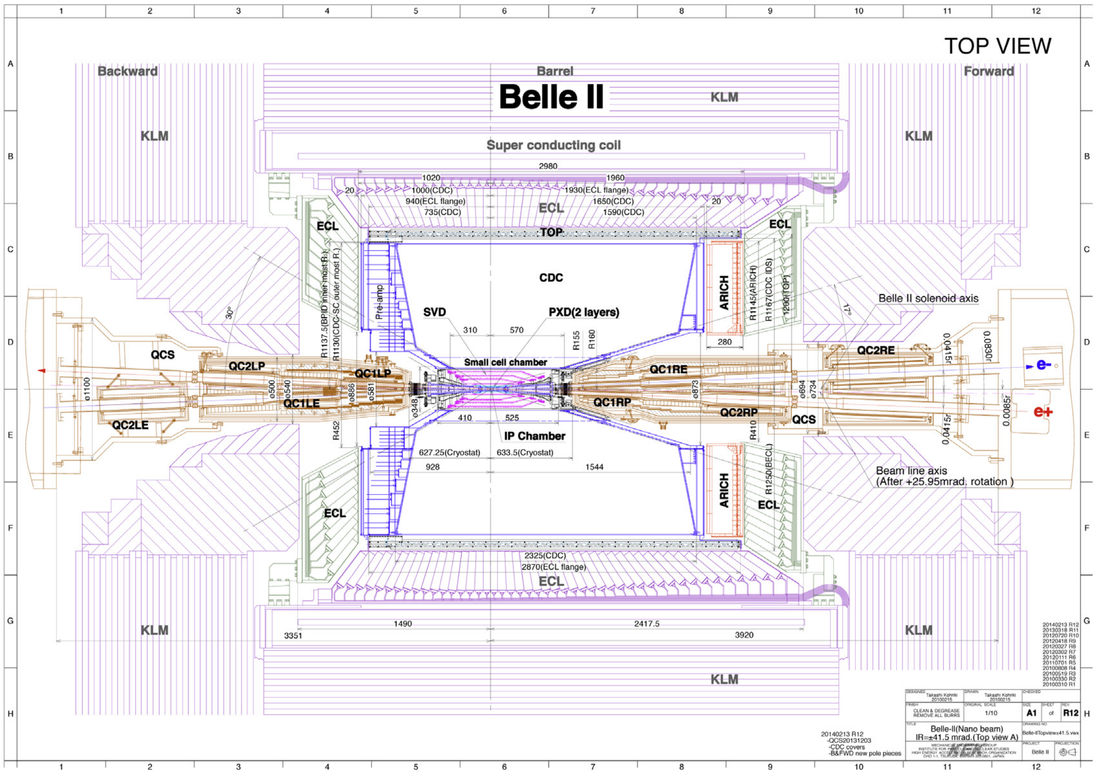


**Fig. 1.** Belle II top view.

**Table 1**
Summary of the Belle II detector components; FWD and BWD stand for forward and backward end-caps.

| Purpose | Name | Component | Configuration | Readout channel count | $\theta$ coverage |
|---|---|---|---|---|---|
| Beam pipe | | Beryllium | Cylindrical, inner radius 10 mm, 10 μm Au, 0.6 mm Be, 1 mm paraffin, 0.4 mm Be | | |
| Tracking | PXD | Silicon Pixel (DEPFET) | Two layers, L1 at radius 14 mm, L2 at 22 mm<br>Sensor size by layer: 12.5 × (L1 44.8, L2 61.44) mm$^2$<br>Pixel size by layer: 50 × (L1a 55, L1b 60, L2a 70, L2b 85) μm$^2$ | 7.7M | [17°; 150°] |
| | SVD | Silicon Strip (double sided) | Rectangular and trapezoidal, strip pitch: 50(p)/160(n)–75(p)/240(n) μm, with one floating intermediate strip; four layers at radii: 39, 80, 104, 135 mm | 245k | [17°; 150°] |
| | CDC | Drift Chamber | small cell, large cell, 56 layers | 14k | [17°; 150°] |
| Particle ID | TOP | RICH with quartz radiator (DIRC) | Barrel: 16 segments in $\phi$ at $r \sim 120$ cm, 275 cm long, 2 cm thick quartz bars with 4 × 4 channel MCP PMTs | 8k | [31°; 128°] |
| | ARICH | RICH with aerogel radiator | FWD end-cap: 2 × 2 cm thick focusing radiators with different $n$, HAPD photodetectors | 60k | [15°; 34°] |
| Calorimetry | ECL | CsI(Tl) | Barrel: $r = 125 - 162$ cm,<br>end-caps: at $z = -102$ cm and $z = +196$ cm | 6624 (Barrel),<br>1152 (FWD), 960 (BWD) | [12.4°; 31.4°],<br>[32.2°; 128.7°], [130.7°; 155.1°] |
| Muon ID | KLM | barrel: RPCs and scintillator strips | 2 layers with scintillator strips and 13 layers with 2 RPCs | $\theta$ 16k, $\phi$ 16k | [40°; 129°] |
| | KLM | end-caps: scintillator strips | 14 (12) layers of [7–10]×40 mm$^2$ strips in forward (backward) region | 17k | [25°; 40°], [129°; 155°] |

in particle physics has now shifted to the possibility that there may be New Physics that appears in flavor physics. There is a broad range of possibilities including new CP violating (matter–antimatter) asymmetries, unexpected rare decays, and violations of lepton flavor universality in $B$ meson decays or $\tau$ lepton decays. The tool for the next round of discoveries at the next generation electron–positron (super) B-factory SuperKEKB [1] will be the Belle II detector (Fig. 1).

While the new detector clearly fits in the same envelope as its predecessor, the superconducting solenoid magnet with its iron return yoke, all components are either new or considerably upgraded [2]. The CsI(Tl) crystals are re-used although their readout electronics were upgraded.

Compared to Belle, the Belle II detector will be taking data at an accelerator with 40 times higher luminosity, and thus has to be able to operate at 40 times higher physics event rates, as well as with background rates higher by a factor of 10 to 20 [2]. To maintain the excellent performance of the spectrometer, the critical issue will be to mitigate the effects of higher background levels, which lead to an increase in occupancy levels and radiation damage, as well as to fake hits and pile-up noise in the electromagnetic calorimeter, and to neutron induced hits in the muon detection system. Higher event rates also require substantial modifications of the trigger scheme, data acquisition system and computing. In addition, improved hadron identification is needed, and a hermiticity at least as good as in the original Belle detector is required.

The requirements for a *B* factory detector can be summarized as follows. The apparatus should meet the following criteria:

– Excellent vertex resolution (≈100 μm);
– Very high reconstruction efficiencies for charged particles and photons, down to momenta of a few tens of MeV/$c$;
– Very good momentum resolution over the entire kinematic range of the experiment, i.e. up to ∼7 GeV/$c$;
– Precise measurements of photon energy and direction from a few tens of MeV to ≈7 GeV;
– A highly efficient particle identification system to separate pions from kaons, and to identify both electrons and muons over the full kinematic range of the experiment;
– Coverage of (nearly) the full solid angle;
– A fast and efficient trigger system,
– A data acquisition system capable of storing and recording large quantities of data, and,

last but not least, a distributed computing system to analyze the recorded data.

For a significant fraction of the momentum range of interest, the tracking and vertexing resolutions are limited by the effects of multiple scattering in addition to intrinsic resolution. In particular, the vertex detectors must be as close as possible to the collision point and the radiation lengths of their components must be minimized. The design choices made for the Belle II experiment are summarized in Table 1, and are discussed in some detail below. A full discussion can be found in the Technical Design Report (TDR) [2].

## 2. Vertex detector (VXD)

### 2.1. SuperKEKB and interaction point (IP)

In the SuperKEKB accelerator, the vertical beta function at the interaction point (IP) is reduced by a factor of about 20 in a so-called Nano-Beam scheme, providing a luminosity improvement by a factor of about 20. To realize this improvement, the final focus magnets are located much closer to the IP by changing the beam crossing angle from 22 mrad to 83 mrad; such a large crossing angle reduces the so-called "hour-glass effect" and eliminates the need for combined function magnets, which is important for beam-related backgrounds. The other improvement to the luminosity comes from an increase in the beam currents by about a factor of two. In addition, the emittances of the two beams were reduced [1]. To mitigate the emittance growth due to intra-beam Coulomb scattering and the short beam lifetime due to the Touschek effect, the beam energy for the $e^+$ beam is increased from 3.5 GeV to 4.0 GeV. The beam energy for the $e^-$ beam is changed from 8.0 GeV to 7.0 GeV accordingly. As a result, the Lorenz boost factor ($\beta\gamma$) is reduced from 0.42 to 0.28, which is a significant change for measurements involving the *B* meson lifetime. On the other hand, the beam pipe at the interaction region has a radius of 10 mm, which is two-thirds of that in the KEKB case. Therefore, we expect the vertex measurement at Belle II to be better by a factor 2 if compared to Belle. Due to the higher beam current and luminosity, the beam background rates are significantly higher and hence Belle II has been designed for a 30 kHz level 1 trigger rate. Fig. 2 shows a picture of the beam pipe at the IP. The central part is made of pure double-walled beryllium, while the crotch parts are composed of tantalum to shield the detector from electromagnetic particle showers. In order to suppress photon hits from synchrotron radiation induced at the final focus magnet, the inside of the IP beam pipe is coated with a 10 μm thick layer of gold.

The Belle II vertex detector (VXD) is comprised of two devices, the silicon PiXel Detector (PXD) and Silicon Vertex Detector (SVD), with a total of six layers (Fig. 3) around the beam pipe. The PXD makes up the inner two layers at $r = 14$ mm and $r = 22$ mm radii. The SVD constitutes the four outer layers of the VXD, with double-sided silicon strip ladders at radii of 39 mm, 80 mm, 104 mm, and 135 mm, respectively. In comparison, in Belle the outermost vertex detector layer was at a radius of 88 mm [3]. Hence the Belle II SVD has improved capabilities for stand-alone tracking. The sensitive lengths in each of the layers are determined by the required polar angular ($\theta$) acceptance of the tracker ($17^\circ < \theta < 150^\circ$).

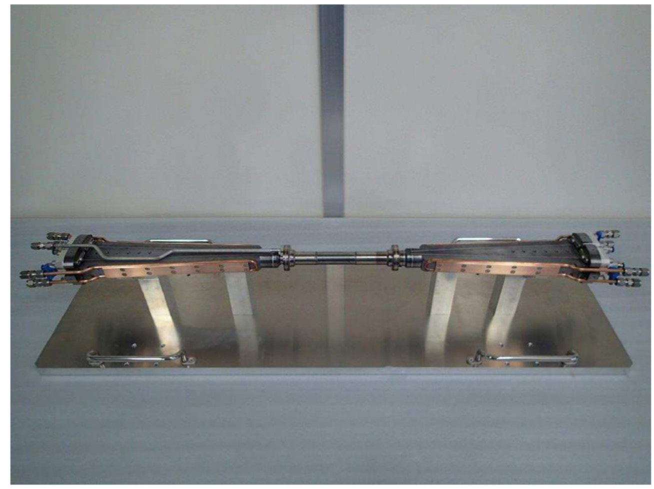

**Fig. 2.** Belle II Beam pipe: the central straight section is made of 1 mm thick pure beryllium and the crotch part is made of tantalum. Its total length is about 900 mm.

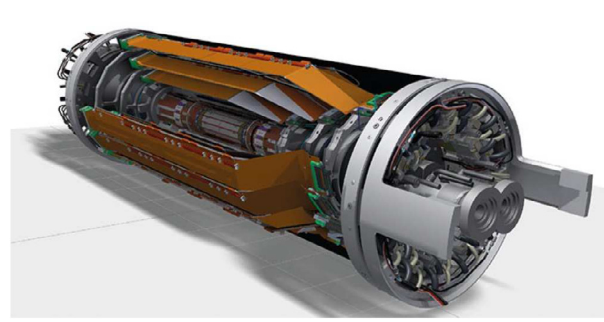

**Fig. 3.** Belle II Vertex Detector: the beam pipe, PXD, SVD, and the shield material are assembled in a single structure.

### 2.2. PXD

The pixel sensor design is based on the DEPleted p-channel Field Effect Transistor (DEPFET) technology [4,5]. A design overview of the PXD is shown in Fig. 4. A DEPFET pixel consists of a fully depleted substrate and is equipped with a p-channel MOSFET structure and with an internal gate where the electrons from the depleted substrate are collected in the local minimum of the electric potential in the pixel. The internal gate modulates the current through the MOSFET on the readout. Thanks to its internal amplification, the DEPFET sensor can be made very thin (75 μm), which minimizes the impact of multiple scattering. The readout electronics consists of three types of ASICs: the Switchers, which switch on a MOSFET pixel row to send the currents; the Drain Current Digitizers (DCD), which digitize the current, and the Data Handling Processor (DHP), which does the zero-suppression of empty pixels and transmits the data stream via the Low Voltage Differential Signaling (LVDS) interfaces. While the Switchers are located along the side of the DEPFET sensor, the DCD and the DHP are located at the ends of the sensors outside of the acceptance region. To reduce the material, the sensor thickness is 75 μm, while the 525 μm thick

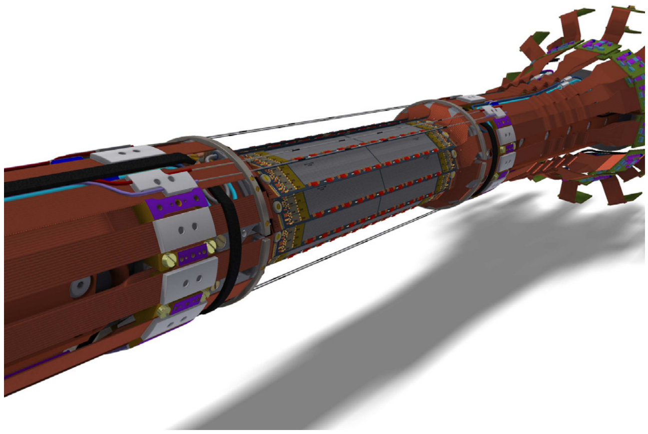

**Fig. 4.** The PXD detector: the DCD and the DHP ASICs are located on each side of sensors. The Switcher ASICs (red block) sit on one side of the ladder, parallel to the beam. (For interpretation of the references to color in this figure legend, the reader is referred to the web version of this article.)

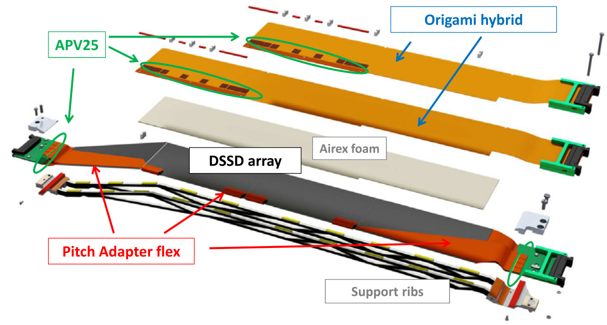


**Fig. 5.** A SVD 5th layer ladder design. The SVD ladder is composed of DSSD sensors, a CFRP rib to support the DSSDs, AIREX foam for electrical isolation, Origami Kapton flex circuits that connect APV25 chips to the central part of the DSSD readout, pitch adapter Kapton flexes and hybrid cards for AVP25 chips for each side of the DSSD readout and connectors.

frame is only partially thinned to keep the ladder mechanically stable. This configuration has an average radiation length of only 0.2%$X_0$. The sensor ladders are mounted on a support cooling block structure, which is attached to the beam pipe. The data from DHPs on each ladder are transmitted to the Data Handling Hybrid (DHH), which is located on the outside of the Belle II detector. The DHH is an FPGA board responsible for initializing the ASICS on the ladder and setting configuration parameters, i.e. the pedestal and threshold values. The data from the DHHs are transmitted to the ONline SElector Node (ONSEN) system, which controls data buffering and transmission of the data following a Region Of Interest (ROI) request based on higher level trigger (HLT) tracking information. For low-momentum tracks, the data concentrator (DATCON) is implemented. The DATCON determines the ROI based on a fast Hough transformation of the SVD hit information. By using the ROI scheme, the volume of the PXD data can be reduced by a factor of about twenty.

At SuperKEKB, continuous beam injection at a rate of 25 Hz for each beam will be used to maintain stable high luminosity operation. In the PXD readout scheme, a four-fold readout in a rolling shutter mode is employed, which requires 20 μs to read a single frame. On the other hand, a single beam revolution takes 10 μs. Consequently, background hits arising from the beam injection can "pile up" with physics. To supress these injection hits, the DEPFET is operated in a "gated" mode [6], which allows us to temporarily blind the detector by setting all "clear" lines to high voltage. By synchronizing this operation with beam injection, electrons from injection background pass the depleted substrate directly through the clear line. Electrons already collected in the pixels are preserved during this blind phase.

### 2.3. SVD

The SVD is made of Double-Sided Silicon micro-strip Detectors (DSSDs); the design is shown in Fig. 5. The double-sided sensors are arranged in such a way that the $n$ side large pitch strips are perpendicular to the beam direction, while small pitch $p$ side strips are parallel to the beam, providing both $x$ and $y$ coordinates of the hits. The innermost SVD layer has small rectangular sensors (thickness: 320 μm). The other three layers are composed of two types of sensors: large rectangular sensors (named barrel sensors, 320 μm) and slanted sensors (300 μm) with a trapezoidal shape, which improves acceptance and precision for forward boosted particles.

Since the luminosity of SuperKEKB is 40 times higher than that of KEKB, the detector design was upgraded to cope with a high rate environment. The hit rate at a radius of 100 mm around the IP, the inner radius of the drift chamber at Belle, would be too high at Belle II. Therefore, the SVD radius coverage is expanded to 135 mm, which allows the SVD to reconstruct the decays of neutral particles such as $K_S^0$ mesons and to track low-momentum particles, such as pions produced in the decay of $D^*$ mesons that do not reach the Central Drift Detector (CDC).

The SVD readout electronics is based on the so-called APV25 chip [7], which was originally developed for the CMS experiment and provides fast readout with a short integration time. The APV25 satisfies all of the requirements on the SVD; a short pulse shaping time (50 ns), pipeline readout for dead time-free operation (with a depth of 192 cells), and radiation tolerance of up to 1 MGy. In order to maintain a high signal-to-noise ratio, the signal line capacitance has to be as small as possible. The so-called "Origami" chip-on-sensor design concept was developed for the Belle II SVD [8], which has thinned APV25 readout ASICs in the active volume of the detector. The average material budget for one ladder including ribs, DSSDs, electronics and cooling pipes is about 0.7% of a radiation length. The analog signals from the APV25 are routed to the so called FADC boards, located on the outside of the Belle II detector, where they are digitized, and pedestal subtraction, common mode noise correction, and zero suppression are carried out.

### 2.4. The VXD cooling

The total power consumption in the PXD system is about 360 W, of which 320 W are dissipated by the DCD/DHP, and 20 W each by sensors and the Switchers. In order to provide effective cooling for the DCD/DHP, the support cooling block has cooling channels inside in the stainless steel structure, which were made using 3D printing. Due to the narrow space between the two layers of the PXD and for effective heat exchange, the Belle II VXD system uses −20 °C liquid $CO_2$ cooling rather than water cooling as in the original Belle vertex detector. For the SVD, the APV25 chips are cooled down to −20 °C with two-phase $CO_2$ flowing inside a thin 1.6-mm diameter pipe that is placed on heat conductive rubber above the APV25; additional cooling is provided through the SVD endrings.

This cooling has two major advantages: it is radiation tolerant and has excellent thermo-mechanical behavior. To avoid water condensation and to further cool the PXD Switcher ASIC, cooled nitrogen gas is blown inside the VXD volume. In total, the heat consumption in the VXD system is about 1 kW. The cooling system for the Belle II VXD is based on the 2-Phase Accumulator controlled Loop (2PACL) method [9], which was originally developed for the thermal control system of the AMS tracker [10], and was later implemented in the LHCb experiment for the cooling of the VErtex LOcator (VELO) [11]. For the Belle II VXD cooling, a new $CO_2$ circulating cooling plant, named IBBelle, was developed in collaboration with the ATLAS group. The cooling concept was also verified at DESY with a full scale thermal mock-up

**Table 2**
Comparison of mechanical parameters between the Belle CDC and the Belle II CDC.

| | Belle II | Belle |
|---|---|---|
| Inner cylinder radius (mm) | 160 | 77 |
| Outer cylinder radius (mm) | 1130 | 880 |
| Number of layers | 56 | 50 |
| Number of sense wires | 14336 | 8400 |

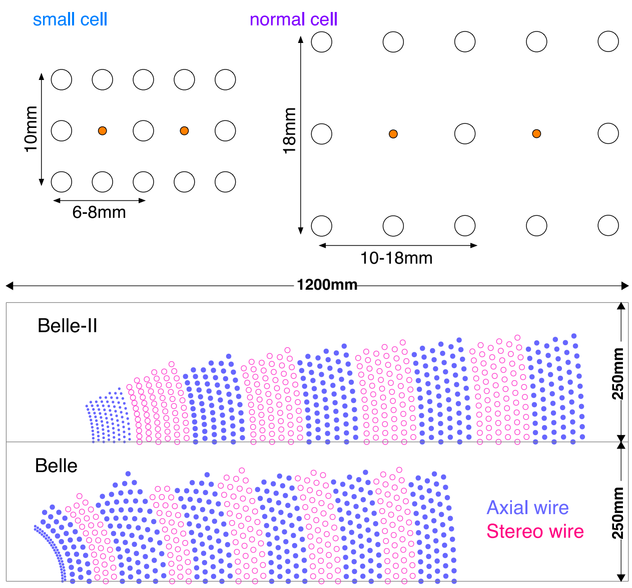


**Fig. 6.** CDC cell dimensions for small and large cells (top); large white and small orange circles denote the cathode and anode wire, respectively. (bottom) Comparison between the wire configurations of the Belle II CDC and the Belle CDC. (For interpretation of the references to color in this figure legend, the reader is referred to the web version of this article.)

## 3. Central Drift Chamber (CDC)

One of the core instruments of the Belle II spectrometer is the central tracking device, a large volume gas drift chamber with small drift cells. The CDC reconstructs the trajectories of charged particles to precisely determine their momenta and provides particle identification in the low-momentum region using energy loss in the CDC volume. In addition, it also generates trigger information for charged particles.

To reduce multiple scattering, the CDC mechanical structure uses low-mass components. The inner and outer cylinders are made of CFRP with thicknesses of 0.4 mm and 5 mm, respectively. Aluminum end-plates with 10 mm thickness are used for both sides. These mechanical components support a 2.3 m long cylindrical structure with 2.2 m diameter [12].

Compared to Belle, the CDC extends to a larger radius, made possible by a much thinner particle ID system in the barrel region. A comparison of the mechanical parameters to the Belle CDC is given in Table 2. To operate at high event rates with increased background levels, the chamber has smaller drift cells than the one used in Belle. In particular, the cell dimensions of the innermost 8 layers are smaller (6–8 mm) than the other layers (10–18 mm), as shown in Fig. 6. The wire configuration is also indicated in Fig. 6.

The anode and cathode wires are gold-plated tungsten wires of 30 μm diameter and aluminum wires of 126 μm diameter, respectively. They are identical to what was used in the Belle CDC; the stable 10-year operation of the Belle CDC motivated this choice. The gas mixture is 50% He–50% $C_2H_6$, the same low-Z gas as used in Belle.

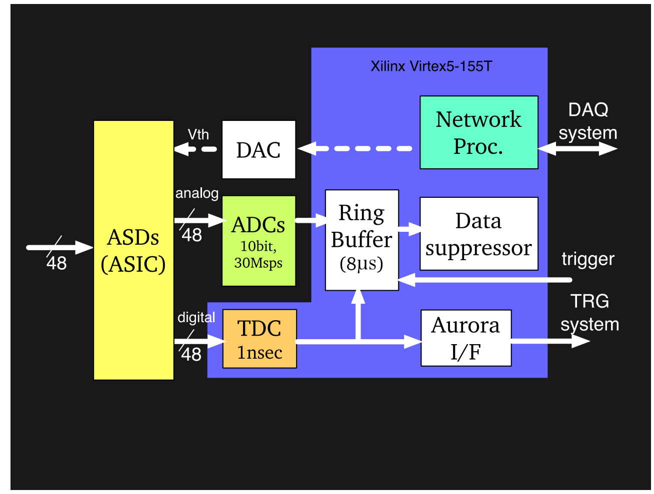


**Fig. 7.** CDC readout block diagram [13].

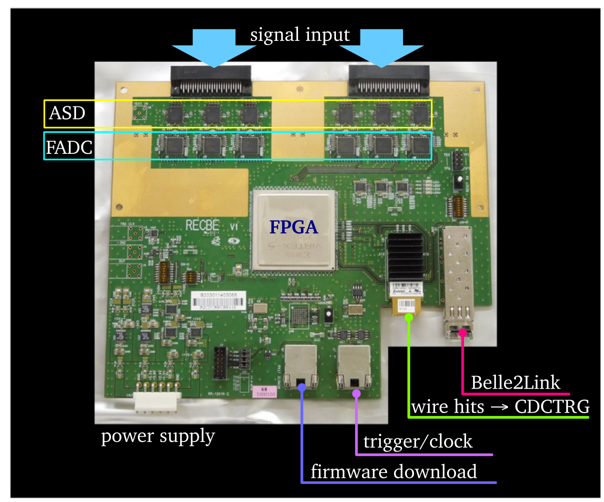


**Fig. 8.** A CDC readout board.

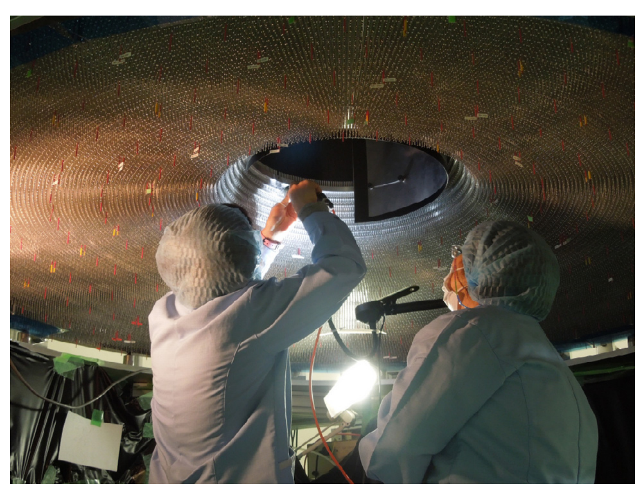

**Fig. 9.** Photograph of the wire stringing for the Belle II CDC.

**Fig. 10.** Belle II CDC installation.

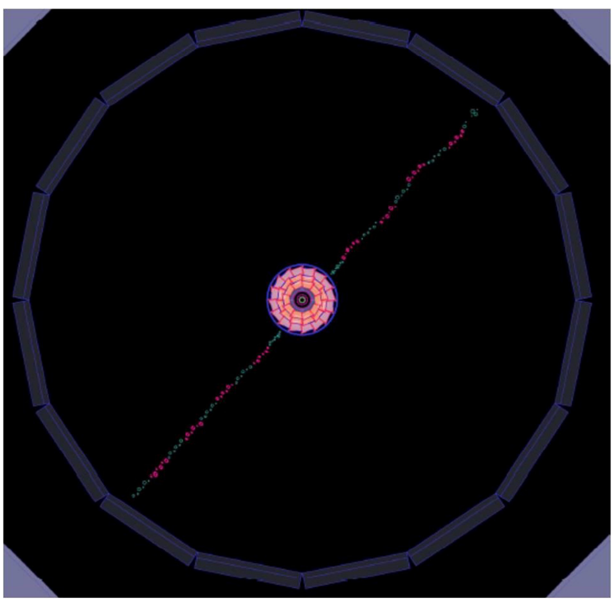

**Fig. 11.** A cosmic ray muon recorded by the Belle II Central Drift Chamber (CDC).

The front-end readout electronics are based on custom-made ASIC chips [14,15], where signal discrimination takes place after amplification and shaping. The ASIC is followed by an FADC, which digitizes signal charge at a rate of 31.25 MHz. The drift time is measured by a TDC with a resolution of 1 ns. The ring buffers are used to store digitized data, and data are transferred to the central DAQ network via RocketIO gigabit transceivers. The CDC readout block diagram is shown in Fig. 7. These readout elements together with the FPGA are instrumented in a single electronics board (Fig. 8). They are placed in the space close to the backward endplate and are water cooled.

Wire stringing started in December 2012, and was completed in January 2014. Fig. 9 shows a photograph of the wire stringing work. For the first 8 layers with small cells, the construction was separately made and installed into the main structure after wire stringing. After tension measurements, cosmic ray tests with a limited number of the readout electronics were carried out. The system was installed in the Belle II structure in October 2016, shown in Fig. 10. Commissioning of the whole system with cosmic rays using the global DAQ system started in July 2017. Fig. 11 shows a cosmic ray muon in the CDC without the solenoid field.

## 4. Particle identification system (TOP and ARICH)

For particle identification in the barrel region, a time-of-propagation (TOP) counter is used [16,17]. This is a special kind of Cherenkov detector in which two-dimensional information about a Cherenkov ring image is given by the time of arrival and impact position of Cherenkov photons at pixelated photo-detectors at one end of a 2.6 m long quartz bar (Figs. 12 and 13). Each detector module (16 in total) consists of a 45 cm wide and 2 cm thick quartz bar with a small expansion volume (about 10 cm long) at the sensor end of the bar. The expansion wedge introduces some additional pinhole imaging, relaxes slightly the precision timing requirements and reduces the hit occupancy at the photo-detector [17]. An important component of the module is also a spherical mirror at the far end of the quartz bar, essential for reducing the chromatic error. At the exit window of the wedge, two rows of sixteen fast multi-anode photon detectors are mounted (Fig. 14). The TOP counter requires photo-sensors with a single photon time resolution of about 100 ps, which can be achieved with a 16-channel MCP (Micro-Channel Plate) PMT [17,18] specially developed for this purpose. For precision timing required in this type of counter, custom-made pipelined waveform sampling read-out electronics is used [19]. Note that for this identification method the starting (particle production) time has to be known with a precision of better than 50 ps; this is indeed challenging, but was already achieved for the time-of-flight (TOF) counter of Belle [20]. The start time is provided by the precision radio-frequency (RF) clock of the SuperKEKB accelerator.

In the forward end-cap region, ARICH, a proximity focusing Cherenkov ring imaging detector with aerogel as the Cherenkov radiator is employed to identify charged particles. The design requirements include a low momentum threshold for pions and good separation of pions and kaons up to about 4 GeV/$c$; for studies of rare $b \to s\ell\ell$ transitions and $B \to D^{(*)}\tau\nu$ decays, it should also be able to separate electrons, muons and pions at momenta below 1 GeV/$c$.

A key parameter of the RICH, the number of detected Cherenkov photons, is increased by a novel method (Fig. 15). Two 2 cm thick layers of aerogel with different refractive indices ($n = 1.045$ upstream, $n = 1.055$ downstream) are used to improve the yield without degrading the Cherenkov angle resolution [21,22]. As the single photon sensitive high granularity sensor, the hybrid avalanche photon detector (HAPD) is used, developed in a joint effort with Hamamatsu [23,24]. In this $73 \times 73$ mm$^2$ sensor with 144 channels, photo-electrons are accelerated through a potential difference of 8 kV, and are then detected in avalanche photodiodes (APD). Sensor production was optimized (thicknesses of $p$ and $p^+$ layers, additional intermediate electrode) following radiation tolerance tests [24] with neutrons and gamma rays. A dedicated ASIC has been developed for the signal readout, which includes an amplifier, a shaper and a differential comparator [25].

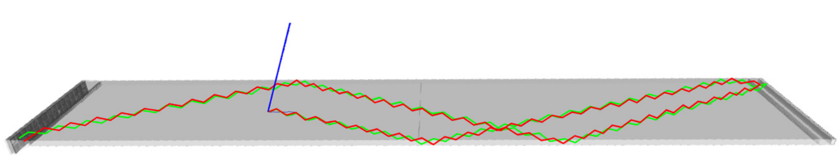

**Fig. 12.** Time-Of-Propagation (TOP) counter, principle of operation: two Cherenkov photon paths, one for a pion (green), and one for a kaon (red) track (shown as a blue line). (For interpretation of the references to color in this figure legend, the reader is referred to the web version of this article.)

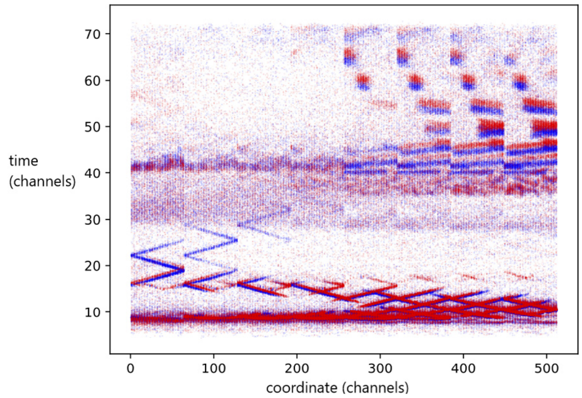


**Fig. 13.** Separation between kaons and pions in the TOP counter: position and time of arrival for detected Cherenkov photons, simulated accumulated patterns for pions (red) and kaons (blue). Eight replicas of the time-vs-coordinate distribution are shown, one for each of the eight rows of the MCP PMT channels, e.g., channels 1 –64 correspond to the top row of channels on the photon detector. (For interpretation of the references to color in this figure legend, the reader is referred to the web version of this article.)

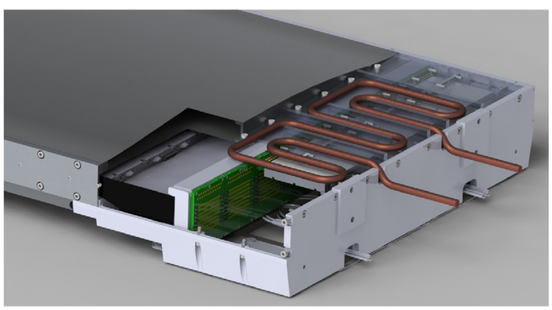

**Fig. 14.** Time-Of-Propagation (TOP) counter read-out box at one end of the quartz bar: back sides of PMTs with electronics read-out boards and cooling.

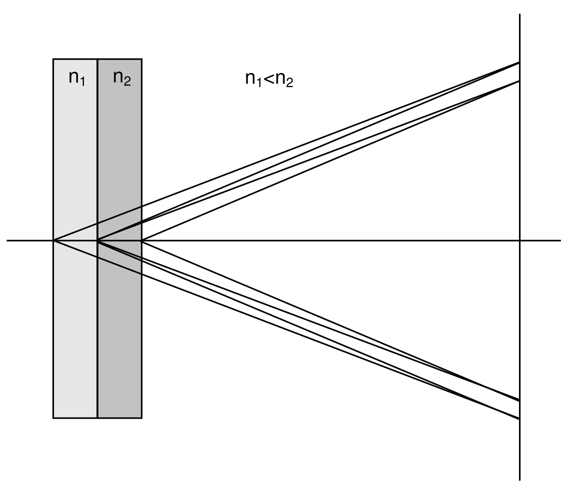


**Fig. 15.** ARICH, the proximity focusing RICH with a non-homogeneous aerogel radiator in the focusing configuration, principle of operation.

All 16 modules of the TOP counter were installed in Belle II in May 2016, and are currently being commissioned [26]. The ARICH detector was constructed in summer 2017 (Fig. 16) and attached to the Belle II spectrometer in autumn 2017. During early commissioning, first Cherenkov rings could be observed (Fig. 17) with a partially instrumented ARICH detector.

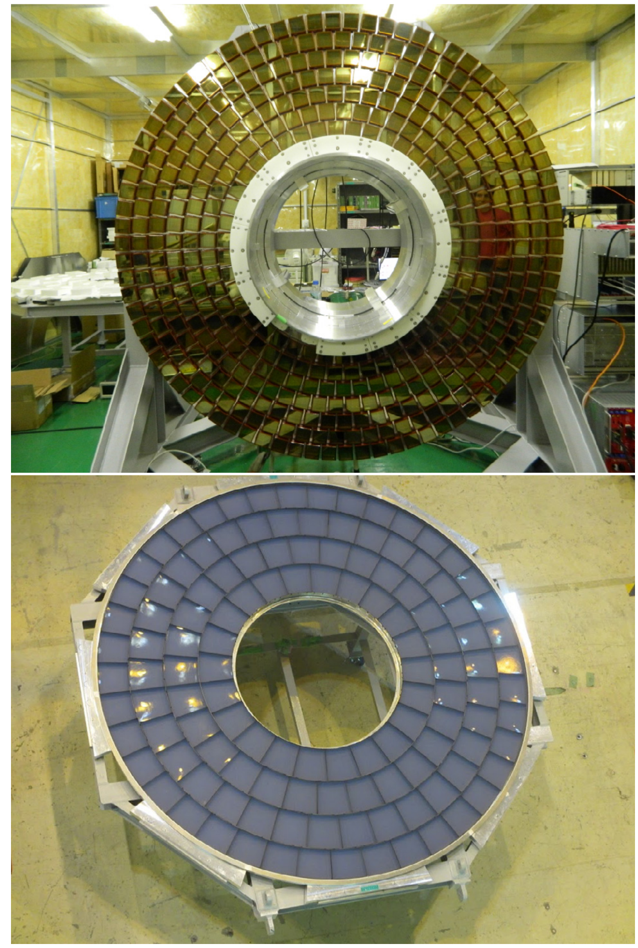

**Fig. 16.** ARICH detector: photon detector plane with HAPD sensors (top), aerogel radiator plane (bottom).

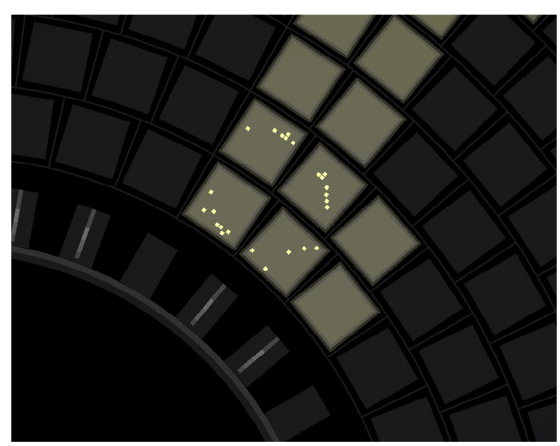

**Fig. 17.** ARICH detector commissioning: a ring produced by a cosmic ray muon.

## 5. Electromagnetic Calorimeter (ECL)

The electromagnetic calorimeter (ECL) is used to detect $\gamma$ rays (photons) over a wide energy range as well as to identify electrons, i.e. separate electrons from hadrons, in particular pions. The ECL is a highly-segmented array of thallium-doped cesium iodide CsI(Tl) crystals assembled in a projective geometry. The mechanical configuration of

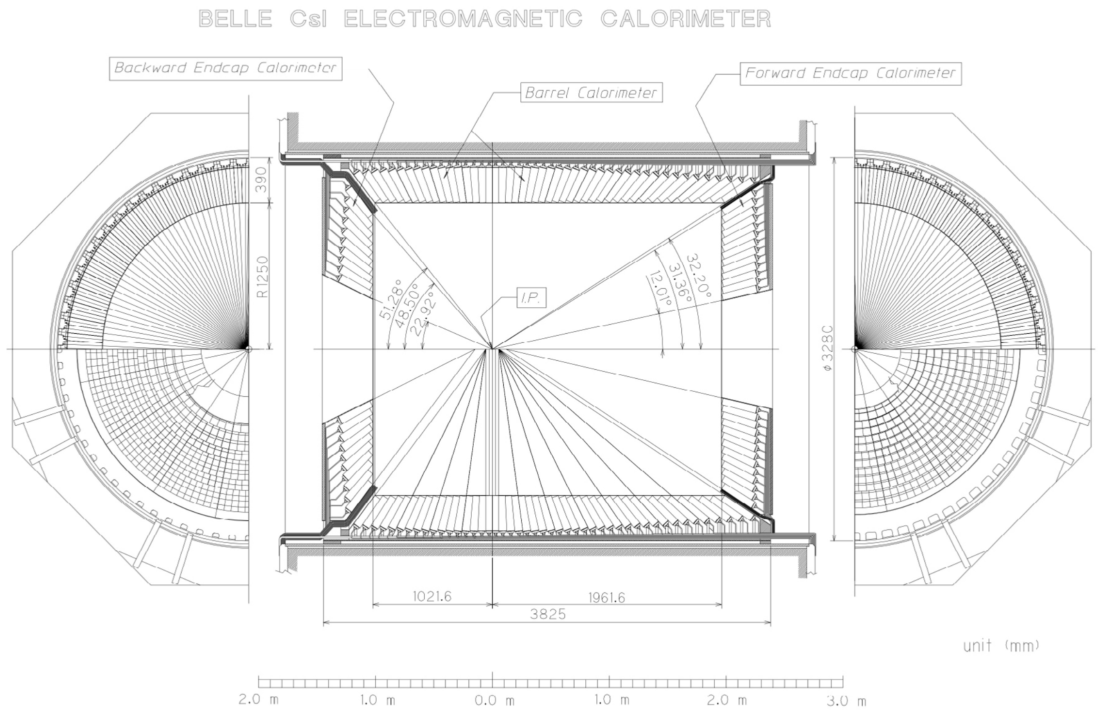


**Fig. 18.** ECL overall configuration.

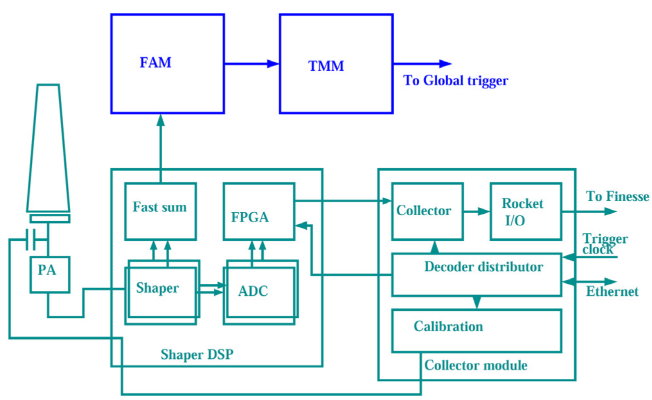


**Fig. 19.** ECL readout block diagram.

**Table 3**
ECL geometrical parameters.

| | $\theta$ coverage | Number of crystals |
|---|---|---|
| Forward end-cap | 12.4 °–31.4° | 1152 |
| Barrel | 32.2 °–128.7° | 6624 |
| Backward end-cap | 130.7 °–155.1° | 960 |

the ECL is shown in Fig. 18. The crystal configuration is unchanged from the Belle calorimeter. All three detector regions, barrel as well as the forward and backward end-caps, are instrumented with a total of 8736 crystals, covering about 90% of the solid angle in the center-of-mass system. Table 3 summarizes the geometrical parameters of the ECL. Each crystal shape is a truncated pyramid, where the average size is 60 mm × 60 mm cross section with a 300 mm length, corresponding to 16.2 $X_0$, for the barrel part. Two photo-diodes, each of which has 10 mm × 20 mm sensitive area, are attached at the back surface of the crystal; signals from the photo-diode are fed to a charge-sensitive amplifier mounted on the crystal together with the photo diode.

In Belle, the energy resolution observed with this calorimeter was $\sigma_E/E = 4\%$ at 100 MeV, 1.6% at 8 GeV, and the angular resolution was 13 mrad (3 mrad) at low (high) energies; $\pi^0$ mass resolution was 4.5 MeV/$c^2$ [27]; in the absence of backgrounds a similar performance would also be expected in Belle II.

However, with the higher background levels expected in Belle II, the relatively long decay time of CsI(Tl) crystals (∼ 1 μs) will considerably increase the overlapping of pulses from neighboring (background) events. To mitigate the resulting large pile-up background, the readout electronics (Fig. 19) have been replaced [28]. This new readout board, called the "Shaper-DSP board", shortens the shaping time to 0.5 μs from 1 μs, and introduces a pipelined readout with waveform sampling analysis, where the raw signal after amplification from each crystal is continuously digitized with a 2 MHz clock frequency. The Shaper-DSP module is shown in Fig. 20. The digitized data are processed by an FPGA when a trigger signal is received. The output data from the Shaper-DSP board are sent to the Collector module, and then are transferred to the Belle II central DAQ via RocketIO gigabit transceivers.

At present, calibration work is ongoing with cosmic ray muon data. For the energy calibration, all crystals in the barrel and the backward have been studied. The hit crystal was selected by requiring energy activity in both neighbors, and a signal from the crystal in question was normalized by the energy value calculated from a Monte Carlo simulation of cosmic ray muon data. Fig. 21 is the normalized energy distribution when both neighbors are located at the same polar angle positions. Reasonable energy resolution was obtained although further analysis is required to optimize the results. ECL timing resolution was also studied. Fig. 22 shows a distribution of the time differences of two counters in the same event with energy deposition between 40 MeV and 80 MeV, corresponding to a single counter time resolution better than 10 ns.

In the forward region of the detector, close to the beam pipe, much higher background rates are expected, so that even with the new waveform sampling electronics the residual pile-up background will degrade the performance. Some further degradation could come from a reduction of the light yield due to radiation damage, although this effect seems to be less significant than originally anticipated [29].

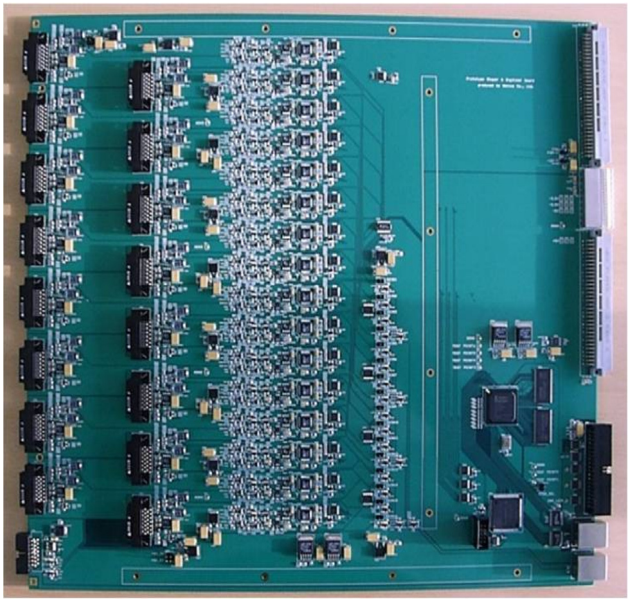

Fig. 20. Photo of the ECL Shaper DSP module.

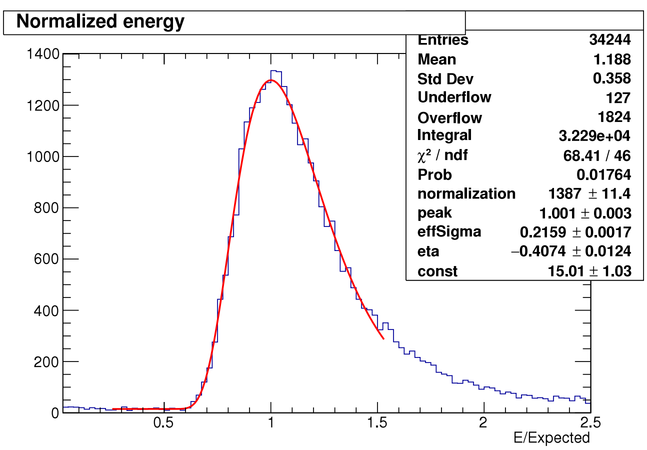


Fig. 21. Energy deposited in the ECL by cosmic ray muons normalized to the expected value.

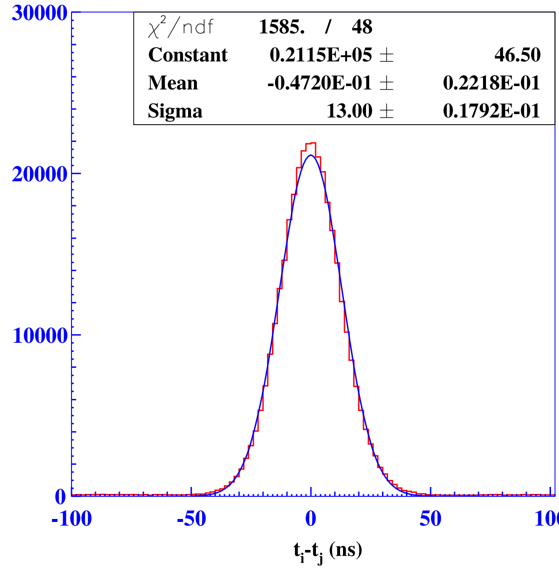


Fig. 22. ECL timing distribution from the Belle II cosmic ray run.

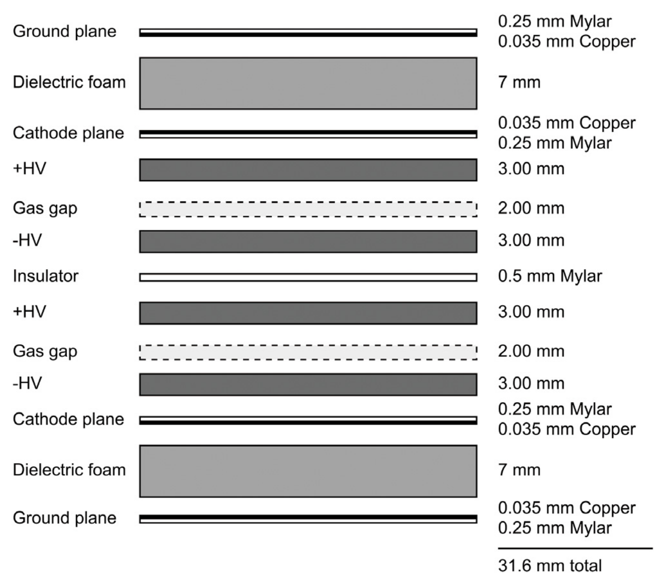


Fig. 23. Resistive place chambers of the KLM system, structure of a super-layer [31].

A possible solution for this region of the spectrometer, a replacement of CsI(Tl) with considerably faster and radiation tolerant pure CsI is under study [30]. Note that pure CsI crystals generate ten times less light than CsI(Tl). Therefore, noise from photo-sensor as well as readout electronics have to be optimized carefully, and radiation hardness up to the level expected with full Belle II luminosity should be confirmed.

## 6. $K_L$- Muon Detector (KLM)

The $K_L$ and muon detector (KLM) consists of an alternating sandwich of 4.7 cm thick iron plates and active detector elements located outside the superconducting solenoid. The iron plates serve as the magnetic flux return for the solenoid. They also provide 3.9 interaction lengths or more of material, beyond the 0.8 interaction lengths of the electromagnetic calorimeter, in which $K_L$ mesons can shower hadronically.

The Belle KLM system, based on glass-electrode resistive plate chambers (RPCs, Fig. 23), demonstrated good performance during the entire data taking period of the Belle experiment. In contrast to Belle, in Belle II large background rates are expected in some portions of the KLM detector system (both endcaps and the innermost layers in the barrel region) due to neutrons that are mostly produced in electromagnetic showers from background processes (e.g., radiative Bhabha scattering). The long dead time of the RPCs due to the recovery of the electric field after a discharge significantly reduces the detection efficiency if the hit rate is large. Because of the high background hit rates, a significant part of the RPC detector system would be completely inefficient, resulting in a large muon misidentification probability [2]. To mitigate this problem, in the critical part of the system (both endcaps and two innermost layers of the barrel region) RPCs have been replaced by layers of scintillator strips with wavelength shifting fibers (Fig. 24), which are tolerant to higher rates. The wavelength-shifted scintillation light is read out by silicon photomultipliers (SiPMs, Geiger mode operated APDs) [32]. Note that the large neutron background will also degrade the SiPMs, and will therefore considerably increase their dark count rate. Irradiation tests have shown, however, that such a detector system can be reliably operated by appropriately shifting the discrimination threshold and/or

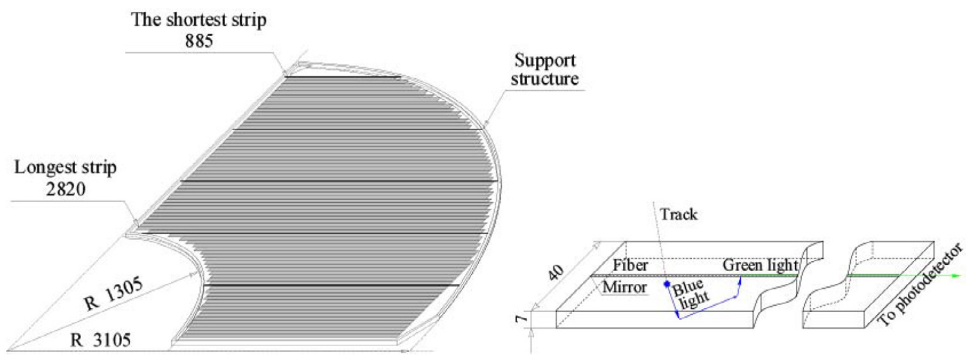


**Fig. 24.** Endcap KLM: single layer formed by scintillator strips (left), scintillator light detection in the strip.

**Table 4**
Main parameters of the solenoid.

| | | |
|---|---|---|
| Cryostat | Inner radius | 1.7 m |
| | Outer radius | 2.0 m |
| Central field | | 1.5 T |
| Nominal current | | 4096 A |
| Stored energy | | 35 MJ |
| Total weight | | 23 ton |
| Coil | Weight | 7.9 ton |
| | Effective radius | 1.8 m |
| | Length | 3.92 m |
| | Cross sections | $3 \times 33$ mm$^2$ |
| | Superconductor | NbTi/Cu |

extracting the local baseline near a signal peak in the readout-ASIC firmware.

## 7. Solenoid and iron structure

An axial magnetic field of 1.5 T is provided by a superconducting solenoid, which is located radially outside of the barrel ECL. The KLM iron yoke functions as a magnetic return circuit. The main parameters in the solenoid are summarized in Table 4. They are the same as in the Belle case [33].

The power supply system of the Belle solenoid was replaced for Belle II. The addition of an iron piece onto the end-yoke structure, which was needed to improve the field shape in the area around final quadrupoles, required a validation of our field mapping model. For this purpose, a solenoid field measurement without the QCS final focus magnets was performed in 2016. To do this, a robotic measuring machine developed at CERN [34] (Fig. 25) was used. This machine consists of a bar, two meters long, on which 34 sensors were attached. Each sensor consists of three Hall probes (one probe in each direction) to determine the three-dimensional magnetic field distribution. This machine moves along the beam direction, azimuthally rotating the sensor bar using pneumatic engines. The path of the probe was programmed remotely via a PC. More than 1.4 million data points were obtained. A detailed field map was obtained after calibration and the results are compared with the computer simulations. The relative difference in the magnetic field strength between measurement and simulation is $\sim$0.1% in most of the CDC volume, which is satisfactory; however, in some areas this difference is up to 0.4

The design of the interaction region of the SuperKEKB accelerator requires a half crossing angle of 41.5 mrad to achieve high luminosity and stable machine operation. To make this possible, the Belle iron platform had to be rotated by 25.9 mrad in the counter-clockwise direction to minimize the effect of the solenoid field on the beam. This rotation work was done during the autumn of 2012 and spring of 2013. The original bogies located under the platform were replaced with new ones that are compatible with the rotation. After the rotation of the Belle structure (including the solenoid, return yoke, KLM system and ECL crystals) the new position was surveyed, examined and verified by the accelerator group. The Belle structure was then rolled out for the installation of the detector sub-systems.

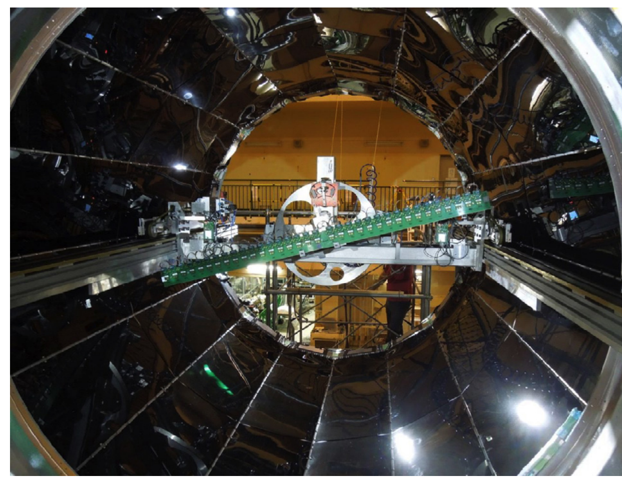

**Fig. 25.** A robotic machine for B field measurement in Belle II.

## 8. Trigger system

The trigger system is responsible for selecting events of interest, while rejecting the large background from intra-beam scattering and Bhabha scattering. The Belle II trigger will be substantially improved over that of Belle, giving a better sensitivity and reduced systematic uncertainty for low multiplicity final states. The main changes are in the level 1 (L1) trigger global decision logic, and in the processing rate of the higher level trigger (HLT). The Belle II trigger will allow triggering on all neutral exotic physics signatures such as $e^+e^- \to \gamma + \text{nothing}$ or $e^+e^- \to \gamma A, (A \to \gamma\gamma)$, where $A$ stands for an Axion-Like-Particle, in the presence of large QED backgrounds. The Belle II trigger will maintain good efficiency, stability and low systematics for 1-prong versus 1-prong $\tau^+\tau^-$ events that provide important input for $g-2$ results.

The requirements for the L1 trigger system are

- high (close to 100%) efficiency (redundancy) for hadronic events from $\Upsilon(4S) \to B\bar{B}$ and $e^+e^- \to q\bar{q}$;
- high efficiency for low multiplicity physics;
- a maximum average trigger rate of 30 kHz;
- a fixed latency of about 5 μs;
- a timing precision of less than 10 ns;
- a minimum two-event separation of 200 ns; and
- a trigger configuration that is flexible and robust.

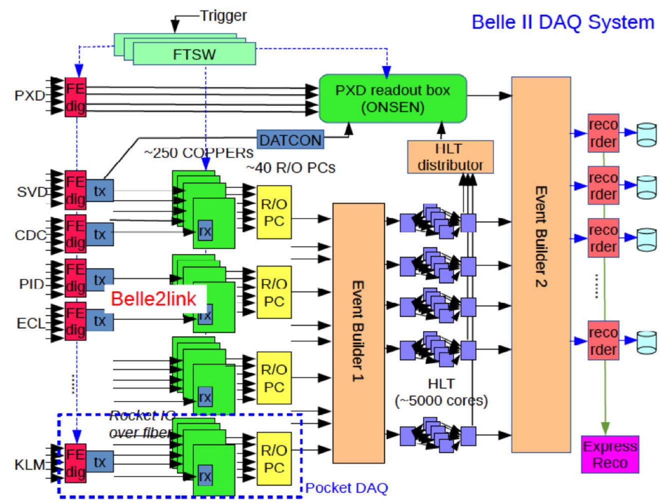


**Fig. 26.** Belle II DAQ system.

## 9. The data acquisition (DAQ) system

The Belle II DAQ transfers detector signals from the front-end electronics of the detector after receiving a L1 trigger. The data from the front-end electronics of each detector subsystem are transferred in parallel from front-end custom readout ASICs to Xilinx FPGA's and then onto High Speed Link Boards (HSLB) through custom high speed (3.125 Gb/s) fiber optic links based on the RocketIO gigabit transceiver GTP protocol (Belle2link), which are followed by the next stage of processing, the COPPER (COmmon Pipeline Platform for Electronics Readout) CPU boards, a common pipelined readout platform, originally developed at KEK. Data from the COPPER boards are combined by event-builder switches to form events and are then transferred to the HLT farm where software triggering and reconstruction can be carried out. The data are then moved to the KEK computing center (KEKCC) for further processing and distribution to the GRID.

The overall scheme is shown in Fig. 26. Data taking without event building is referred to as "PocketDAQ". While most of the subsystems are treated in a uniform manner with feature extraction on the front-end readout boards, it is important to note that due to its large data volume, the readout of the pixel detector (PXD) requires special treatment and sparsification, as already discussed in Section 2.2. SVD track segments are projected into the PXD to determine ROIs (Regions of Interest) using the track information obtained by HLT or using FPGAs in the DATCON modules. Only the data from the ROIs of the PXD are read out, thus reducing the data flow to a level that is acceptable for the second event builder switch.

The FTSW (Front end Timing Switch) system, a tree of custom boards, provides a multiple of the SuperKEKB accelerator RF clock (127 MHz) for system-wide detector readout synchronization. The FTSW distribution system also fans out the trigger signal and several other important fast timing control signals. The timing jitter of the FTSW is in the 20–30 ps range.

The Belle II DAQ is designed to handle a maximum trigger rate of 30 kHz, the value expected at full luminosity from all physics processes and beam-related background. A safety factor of 50% has been included in this value. The typical size of a hadronic event is 100 kbytes.

## 10. Computing and software

The same software framework is used for data acquisition, simulation, reconstruction, and analysis. It executes a series of dynamically loaded modules written in C++ and is configured by a python script. Modern multi-core CPUs are exploited by its parallel processing feature.

For the simulation, several generators, including EvtGen [35], are integrated and Geant4 [36] is used to simulate the detector response. Beam background can either be mixed to simulated signal events before digitization using simulated background of various types or by overlaying random trigger events after digitization.

Two strategies, a global Legendre finder and a local segment finder, are used to find track candidates in the CDC. A stand-alone SVD tracking is based on a cellular automaton technique. Combined tracks are build by merging CDC and SVD candidates and by extrapolating CDC tracks to the SVD. Finally PXD hits are attached. The track parameters are determined with genfit [37] for multiple particle type hypotheses. The reconstruction in the charged particle identification detectors yields likelihoods for the electron, muon, pion, kaon, proton, and deuteron hypothesis. A global PID is given by the sum of log likelihoods. The identification of muons mainly relies on the extrapolation of tracks into the KLM detector with Geant4e. The higher level of background in the ECL compared to Belle required the design of a new cluster reconstruction algorithm which considers multiple particle hypotheses.

A modular analysis framework provides standard functions on steering file level for common analysis tasks such as building particle combinations, vertex fitting, or flavor tagging. These tasks are configured with human readable strings that describe the decay chains. A flexible system is implemented to write out ntuples with the information relevant for specific analyses.

Belle II large scale computing follows the GRID model developed by the LHC experiments and uses the computing resources of the 25 Belle II member nations. A series of Monte Carlo (MC) campaigns have been carried out in which large quantities of events are generated, simulated and reconstructed. The GRID computing system and jobs are managed using the DIRAC (Distributed Infrastructure with Remote Agent Control) interware, which was originally developed by the LHCb experiment. Powerful high level monitoring tools allow the tracking of hundreds of thousands of jobs and files across the globe.

As the Belle II data production system evolves and the Belle II reconstruction software as well as the beam background simulation rapidly improves, there is a need to re-generate the Monte Carlo samples.

So far there have been nine GRID MC campaigns in Belle II. During each campaign the equivalent of 1 to 5 ab$^{-1}$ integrated luminosity has been generated depending on the changes to the software preceding the campaign and the needs for physics analysis.

In these campaigns, the underlying physics processes $e^+e^- \to u\bar{u}, d\bar{d}, s\bar{s}, c\bar{c}$, $e^+e^- \to \tau^+\tau^-$ and $e^+e^- \to \Upsilon(4S)$ are generated in proportion to their cross-sections. Samples with and without beam background are also produced to verify the robustness of the detector reconstruction software. Special signal samples are generated based on requests from the physics study groups. Samples of QED backgrounds, which have very large cross-sections but are either pre-scaled or suppressed by Belle II triggers are also prepared. Various skims from the large MC campaigns are produced including one containing fully reconstructed B meson tags, which is needed for studies of "missing energy decays".

The output of each GRID MC campaign is used to test physics analyses and measure performance of the reconstruction packages. Following MC8 (the 8th GRID campaign), user analysis has started on the GRID.

In addition to the GRID campaigns, there are "dress rehearsals" to test the data flow starting from raw data and check the functionality of the DAQ and HLT (High Level Trigger) as well as transfer to the Tier-0 computing facility of KEK.

## 11. Expected detector performance

The performance of Belle II is yet to be evaluated since both parameter tuning of detector hardware and development of software are still ongoing. In general, the performance is expected to be as good as, or better than in the Belle case despite the much worse beam background environment.

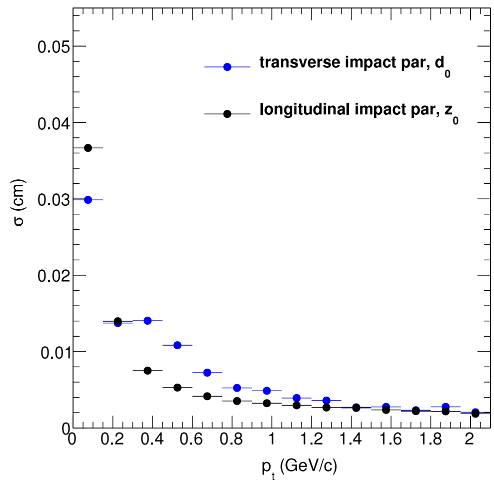


**Fig. 27.** Transverse and longitudinal IP resolution as a function of transverse momentum as determined on simulated data.

Thanks to a smaller radius beam pipe of 1.0 cm rather than 1.5 cm, the first layer of the vertex detector can be placed as close as 1.4 cm to the interaction point, which enables much better impact parameter resolution (Fig. 27) if compared to the values achieved at Belle.

New particle identification devices together with characteristic energy loss in the tracking detectors result in a better particle discrimination power than Belle. Fig. 28 shows the expected pion identification efficiency and kaon misidentification rate. In Belle, kaons of momentum $p = 2\,\mathrm{GeV}/c$ are identified with efficiency of 85% with 10% pion mis-identification rate. In Belle II, the expected performance is 90% kaon efficiency with 4% mis-identification probability for the same momentum.

Charged track momentum resolution is also improved thanks to the longer lever arm of the Belle II CDC. A transverse momentum resolution of $\sigma_{p_t}/p_t = 0.0013 p_t\ [\mathrm{GeV}/c] \oplus 0.0030/\beta$ is obtained for cosmic ray muons even though a great deal of extra material from a magnetic field mapper was inside the CDC. With improved alignment and without the extra material, the resolution is expected to improve to $\sigma_{p_t}/p_t = 0.0011 p_t\ [\mathrm{GeV}/c] \oplus 0.0025/\beta$. However, the impact of beam background must be carefully investigated.

The energy resolution of photons reconstructed by ECL is as good as in Belle when the beam background level is low, however, it could be degraded at low energies in the presence of high beam background as shown in Fig. 29. Therefore, beam background must be mitigated and kept under control by careful machine optics parameter tuning, collimator tuning, and implementation of beam background shields in appropriate locations.

Table 5 summarizes the basic performance of Belle II in comparison to Belle. More details of Belle and Belle II performance can be found elsewhere [2,31,38].

## 12. Detector construction and commissioning status

The detector construction and commissioning proceeds roughly according to the plan. The TOP counter was installed in spring and early summer 2016, and the CDC was installed in October 2016. The detector was transported to its final in-beam position ("roll-in") in April 2017. In

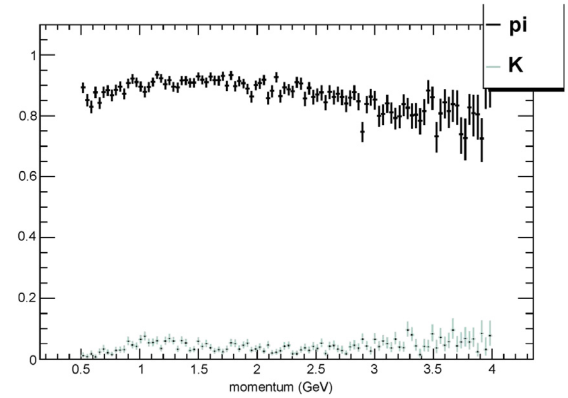


**Fig. 28.** Pion identification efficiency and kaon mis-identification rate as a function of momentum, determined on simulated event samples.

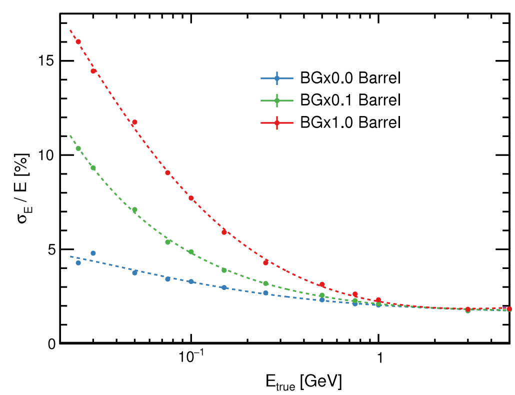


**Fig. 29.** Belle II ECL energy resolution, simulated data with and without beam background.

summer 2017 the detector was partly commissioned in a global cosmic ray run. In fall 2017 the two forward detectors, ARICH and forward endcap ECL, were added. The vertex detector will be installed in summer 2018.

The Belle II experiment is scheduled to begin its first "physics" run in February 2019, after having gone through two commissioning periods known as "Phase 1" (February 2016–June 2016) and "Phase 2" (March 2018–July 2018). For both phases a collection of detectors, known as BEAST 2 (Beam Exorcism for A Stable Belle II Experiment) was installed close to the interaction point for measuring background rates and operating conditions. During Phase 1, the solenoid and the superconducting final focus magnets were not on the beam line, and no collisions took place [39]. However, for Phase 2 all subsystems except for the final vertex detectors will be ready, and the opportunity exists for colliding beams to produce useful physics and calibration events.

## 13. Summary

*B* factories have proven to be an excellent tool for flavor physics, with reliable long term operation and constant improvements, achieving and surpassing design performance. They have contributed to a major step in our understanding of flavor, an important part of the Standard Model. They continue to provide new insight from the analysis of the final data sets, concentrating on measurements that use the unique capabilities of *B* factories.

The construction of a next generation experiment, a super *B* factory is being finalized at KEK, with the SuperKEKB accelerator and the Belle II detector. The commissioning of the accelerator has started in January

**Table 5**
Summary of detector performance.

| Measurement | Belle | Belle II |
|---|---|---|
| $B$ Vertex Reconstruction (typical) | $\sigma_z = 61\,\mu\mathrm{m}$ | $\sigma_z = 26\,\mu\mathrm{m}$ |
| Tracking | $\sigma_{p_t}/p_t = 0.0019 p_t\ [\mathrm{GeV}/c] \oplus 0.0030/\beta$ | $\sigma_{p_t}/p_t = 0.0011 p_t\ [\mathrm{GeV}/c] \oplus 0.0025/\beta$ |
| $K\pi$ ID | Kaon efficiency $\epsilon_K \simeq 0.85$ with pion fake rate $\epsilon_\pi \simeq 0.10$ for $p = 2\,\mathrm{GeV}/c$ | $\epsilon_K \simeq 0.90$ with $\epsilon_\pi \simeq 0.04$ for $p = 2\,\mathrm{GeV}/c$ |
| Calorimetry | $\frac{\sigma_E}{E} = \frac{0.066\%}{E} \oplus \frac{0.81\%}{\sqrt[4]{E}} \oplus 1.34\%$ | $\frac{\sigma_E}{E} = 7.7\%$ at 0.1 GeV, 2.25% at 1 GeV (Fig. 29) |
| Muon ID | Muon efficiency $\epsilon_\mu \simeq 0.90$ with fake rate $\epsilon \simeq 0.02$ for $p_t > 0.8\,\mathrm{GeV}/c$ tracks | $\epsilon_\mu = 0.92 - 0.98$ with $\epsilon = 0.02 - 0.06$ for $p > 1\,\mathrm{GeV}/c$ |
| L1 Trigger | 500 Hz typical average, Efficiency for hadronic events $\epsilon_{\mathrm{hadron}} \simeq 1$ | 30 kHz max. average rate, $\epsilon_{\mathrm{hadron}} \simeq 1$ |
| DAQ | ~5% dead time at 500 Hz L1 rate | <3% dead time at 30 kHz L1 rate |

2016, and the detector will be ready for data taking early in 2018. With this second generation $B$ factory, we can expect a new and exciting era of discoveries, complementary to the LHC.


## Acknowledgements

We would like to acknowledge the great contributions of the physicists, engineers and students from the 25 member nations and regions of the Belle II experimental collaboration and the support of their national funding agencies.


## References


[1] Yukiyoshi Ohnishi, et al., Accelerator design at SuperKEKB, PTEP 2013 (2013) 03A011.
[2] T. Abe, et al., Belle II Technical Design Report, 2010, arXiv:1011.0352.
[3] Z. Natkaniec, et al., Status of the Belle silicon vertex detector, in: Proceedings, 13th International Workshop on Vertex Detectors (Vertex 2004): Menaggio, Como, Italy, September 13-18, 2004, Nucl. Instrum. Methods A560 (2006) 1–4.
[4] J. Kemmer, E. Belau, U. Prechtel, W. Welser, G. Lutz, Low capacity drift diode, Nucl. Instrum. Methods A253 (1987) 378–381.
[5] P. Fischer, et al., Progress towards a large area, thin DEPFET detector module, in: Vertex detectors. Proceedings, 15th International Workshop, VERTEX 2006, Perugia, Italy, September 25-29, 2006, Nucl. Instrum. Methods A582 (2007) 843–848.
[6] L. Andricek, et al., Laser tests of the DEPFET gated operation, in: Proceedings, Topical Workshop on Electronics for Particle Physics (TWEPP12): Oxford, UK, September 17-21, 2012, JINST 8 (2013) C01051.
[7] M.J. French, et al., Design and results from the APV25, a deep sub-micron CMOS front-end chip for the CMS tracker, in: Development and application of semiconductor tracking detectors. Proceedings, 4th International Symposium, Hiroshima, Japan, March 22-25, 2000, Nucl. Instrum. Methods A466 (2001) 359–365.
[8] Gagan B. Mohanty, Belle II Silicon vertex detector, in: Proceedings, 10th International 'Hiroshima' Symposium on the Development and Application of Semiconductor Tracking Detectors (HSTD-10): Xian, China, September 25-29, 2015, Nucl. Instrum. Methods A831 (2016) 80–84 arXiv:1511.06197.
[9] Bart Verlaat, Auke-Pieter Colijn, CO(2) cooling developments for HEP detectors, in: Proceedings, 18th International Workshop on Vertex detectors and related techniques (VERTEX 2009): Putten, Netherlands, September 13-18, 2009, PoS VERTEX2009 (2009) 031.
[10] D. Haas, The silicon tracker of AMS02, in: Proceedings, 6th International Conference on Large Scale Applications and Radiation Hardness of Semiconductor Detectors (RD03): Florence, Italy, September 29-October 1, 2003, Nucl. Instrum. Methods A530 (2004) 173–177.
[11] M.G. van Beuzekom, LHCb VELO Collaboration, Status and prospects of the LHCb vertex locator, in: Large scale applications and radiation hardness of semiconductor detectors. Proceedings, 8th International Conference, Florence, Italy, June 27, 2007, Nucl. Instrum. Methods A596 (2008) 21–24.
[12] N. Taniguchi, Belle II Collaboration, Central drift chamber for Belle II, in: Proceedings, International Conference on Instrumentation for Colliding Beam Physics (INSTR17): Novosibirsk, Russia, JINST 12 (06) (2017) C06014.
[13] Tomohisa Uchida, Masahiro Ikeno, Yoshihito Iwasaki, Masatoshi Saito, Shoichi Shimazaki, Manobu Tanaka, Nanae Taniguchi, Shoji Uno, Readout electronics for the central drift chamber of the Belle II detector, IEEE Trans. Nucl. Sci. 62 (2015) 1741–1746.
[14] Nanae Taniguchi, Masahiro Ikeno, Yoshihito Iwasaki, Masatoshi Saito, Shoichi Shimazaki, Manobu Tanaka, Tomohisa Uchida, Shoji Uno, All-in-one readout electronics for the Belle II Central Drift Chamber, in: Proceedings, 13th Vienna Conference on Instrumentation (VCI 2013): Vienna, Austria, February 11-15, 2013, Nucl. Instrum. Methods A732 (2013) 540–542.
[15] Shoichi Shimazaki, Takashi Taniguchi, Tomohisa Uchida, Masahiro Ikeno, Nanae Taniguchi, Manobu M. Tanaka, Front-end electronics of the Belle II drift chamber, Nucl. Instrum. Methods A735 (2014) 193–197.
[16] M. Akatsu, et al., Time of propagation Cherenkov counter for particle identification, Nucl. Instrum. Methods A440 (2000) 124–135 arXiv:physics/9904009.
[17] M. Starič, K. Inami, P. Križan, T. Iijima, Likelihood analysis of patterns in a time-of-propagation (TOP) counter, in: Proceedings, 6th International Workshop on Ring Imaging Cherenkov Detectors (RICH 2007), Nucl. Instrum. Methods A595 (2008) 252–255.
[18] M. Akatsu, et al., MCP-PMT timing property for single photons, Nucl. Instrum. Methods A528 (2004) 763–775.
[19] Larry L. Ruckman, Gary S. Varner, Sub-10ps Monolithic and Low-power Photodetector Readout, Nucl. Instrum. Methods A602 (2009) 438–445 arXiv:0805.2225.
[20] H. Kichimi, et al., Belle Collaboration, KEKB beam collision stability at the picosecond timing and micron position resolution as observed with the Belle Detector, JINST 5 (2010) P03011 arXiv:1001.1194.
[21] S. Korpar, T. Iijima, et al., A novel type of proximity focusing RICH counter with multiple refractive index aerogel radiator, Nucl. Instrum. Methods A548 (2005) 383–390 arXiv:physics/0504220.
[22] Peter Križan, Samo Korpar, Toru Iijima, Study of a nonhomogeneous aerogel radiator in a proximity focusing RICH detector, Nucl. Instrum. Methods A565 (2006) 457–462 arXiv:physics/0603022.
[23] Shohei Nishida, Ichiro Adachi, Toru Iijima, Hirokazu Ikeda, Samo Korpar, Peter Križan, Yuichi Miyazawa, Isao Nishizawa, Takayuki Sumiyoshi, Development of an HAPD with 144 channels for the aerogel RICH of the Belle upgrade, in: Proceedings, 6th International Workshop on Ring Imaging Cherenkov Detectors (RICH 2007), Nucl. Instrum. Methods A595 (2008) 150–153.
[24] S. Nishida, et al., Aerogel RICH for the Belle II forward PID, in: Proceedings, 8th International Workshop on Ring Imaging Cherenkov Detectors (RICH 2013), Nucl. Instrum. Methods A766 (2014) 28–31.
[25] Shohei Nishida, et al., Development of the readout ASIC for the 144 channel HAPD for aerogel RICH, in: Technology and instrumentation in particle physics. Proceedings, 1st International Conference, TIPP09, Tsukuba, Japan, March 12-17, 2009, Nucl. Instrum. Methods A623 (2010) 504–506.
[26] J. Fast, Belle II Barrel Particle Identification Group Collaboration, The Belle II imaging Time-of-Propagation (iTOP) detector, in: Proceedings, 9th International Workshop on Ring Imaging Cherenkov Detectors (RICH 2016): Bled, Slovenia, September 5-9, 2016, Nucl. Instrum. Methods A876 (2017) 145–148.
[27] A.J. Bevan, et al., The Physics of the B Factories, Eur. Phys. J. C74 (2014) 3026 arXiv:1406.6311.
[28] V. Aulchenko, A. Bobrov, T. Ferber, A. Kuzmin, K. Miyabayshi, G. de Nardo, V. Shebalin, A. Sibidanov, Yu. Usov, V. Zhulanov, Time and energy reconstruction at the electromagnetic calorimeter of the Belle II detector, in: Proceedings, International Conference on Instrumentation for Colliding Beam Physics (INSTR17): Novosibirsk, Russia, JINST 12 (08) (2017) C08001.
[29] Savino Longo, John Michael Roney, Radiation hardness of 30 cm Long CsI(Tl) Crystals, JINST 11 (08) (2016) P08017 arXiv:1608.07556.
[30] A. Kuzmin, Belle ECL Collaboration, Endcap calorimeter for SuperBelle based on pure CsI crystals, in: Technology and instrumentation in particle physics. Proceedings, 1st International Conference, TIPP09, Tsukuba, Japan, March 12-17, 2009, Nucl. Instrum. Methods A623 (2010) 252–254.
[31] A. Abashian, et al., The Belle detector, Nucl. Instrum. Methods A479 (2002) 117–232.
[32] V. Balagura, M. Danilov, B. Dolgoshein, S. Klemin, R. Mizuk, P. Pakhlov, E. Popova, V. Rusinov, E. Tarkovsky, I. Tikhomirov, Study of scintillator strip with wavelength shifting fiber and silicon photomultiplier, Nucl. Instrum. Methods A564 (2006) 590–596 arXiv:physics/0504194.
[33] Y. Makida, H. Yamaoka, Y. Doi, J. Haba, F. Takasaki, A. Yamamoto, Development of a superconducting solenoid magnet system for the B factory detector (BELLE), in: Proceedings, Cryogenic Engineering Conference (CEC 1997) Portland, Oregon, July 28 - August 1, 1997, Adv. Cryog. Eng. 43 (1998) 221–228.
[34] M. Aleksa, et al., Measurement of the ATLAS solenoid magnetic field, JINST 3 (2008) P04003.
[35] D.J. Lange, The EvtGen particle decay simulation package, in: Proceedings, 7th International Conference on B physics at hadron machines (BEAUTY 2000): Maagan, Israel, September 13-18, 2000, Nucl. Instrum. Methods A462 (2001) 152–155.
[36] S. Agostinelli, et al., GEANT4 Collaboration, GEANT4: A simulation toolkit, Nucl. Instrum. Methods A506 (2003) 250–303.

[37] J. Rauch, et al. GENFIT - a generic track-fitting toolkit, 2014, arXiv:1410.3698.
[38] Jolanta Brodzicka, et al., Belle Collaboration, Physics achievements from the Belle experiment, PTEP 2012 (2012) 04D001 arXiv:1212.5342.
[39] A. Aloisio, et al., First measurements of beam backgrounds at SuperKEKB, Nucl. Instrum. Methods (2018) submitted for publication.